

SUPERSONIC GROUND EFFECT AERODYNAMICS OF A SLENDER BODY

Yiyuan Xun[1], Qiulin Qu[1] & Peiqing Liu[1]

[1]Beihang University, Beijing, 100191, People's Republic of China

Abstract

This study investigates the supersonic ground-effect aerodynamics of a high-fineness-ratio slender body of revolution using steady compressible Reynolds-averaged Navier–Stokes simulations. Six representative Mach numbers, covering low- to high-supersonic regimes, are considered at different ground clearances. Variations in aerodynamic forces, surface-pressure distributions, and shock-surface structures are analyzed to clarify the underlying flow mechanisms. The results show that, as the height decreases, the lift first increases to a positive peak and then decreases; at lower supersonic Mach numbers, it may even become negative at small clearances. In contrast, the drag variation is relatively weak except at very small heights. Flowfield analysis indicates that these aerodynamic trends are governed by successive shock reflections between the body and the ground, together with pronounced diffraction of the ground-reflected shock around the body. These three-dimensional shock interactions induce circumferential pressure redistribution and strongly affect the lift and pitching-moment characteristics.

Keywords: ground effect, supersonic flow, slender body of revolution, aerodynamic characteristics.

1. Introduction

When a vehicle flies close to the ground or a water surface, the surrounding flowfield and aerodynamic forces are affected by the underlying surface; this phenomenon is commonly referred to as ground effect (GE). Most previous studies of GE aerodynamics have focused on the subsonic regime [1,2]. With the development of high-speed vehicles, transonic and supersonic GE phenomena have been widely observed for slender bodies such as missiles and projectiles [3,4]. In high-speed GE of slender bodies, body-generated shock waves may reflect from the ground and interact again with the body, producing aerodynamic behaviors that differ fundamentally from those observed in low-speed GE.

For two-dimensional high-speed GE aerodynamics, compressibility effects and shock/expansion-wave interactions are of primary importance [3]. Doig et al. [5] and Gao et al. [6] investigated the transonic GE of the RAE2822 airfoil. Their results showed that, as height decreases, the upper-surface shock moves upstream and the lift may initially increase; however, further height reduction can induce a lower-surface shock, leading to lift loss and drag rise. Jiang et al. [7] studied the choking limit of diamond airfoils in supersonic GE and showed that choking can expel the shock system from the airfoil–ground channel and form a detached bow shock upstream, producing a sharp pressure rise near the lower-surface leading edge.

For three-dimensional high-speed GE, several studies have examined the aerodynamic characteristics of relatively low-fineness-ratio projectiles. Carriage et al. [8] and Doig et al. [9] investigated transonic projectile GE using numerical simulations and showed that ground proximity can significantly modify the force, moment, and surface-pressure distributions. At small heights, the ground-normal force and pitching moment may change markedly, thereby affecting the projectile trajectory response. Doig et al. [10] further studied a supersonic projectile in proximity to a solid surface at Ma = 2.4. Their results identified distinct types of shock–ground interactions as the height decreased, together with pronounced three-dimensional shock reflections and wake distortions. These shock–ground interactions were shown to significantly increase drag and generate strong

https://doi.org/10.71945/icas2026_0598

ground-normal forces, highlighting the complexity of supersonic GE aerodynamics. Sheridan et al. [11] subsequently clarified the Mach-number dependence of projectile GE, showing that the height range affected by GE decreases with increasing Mach number. Overall, existing studies on three-dimensional high-speed GE have mainly emphasized the aerodynamic effects of body-generated shocks after reflection from the ground, particularly their subsequent impingement on the body and the associated secondary reflections and pressure changes. Related steady three-dimensional shock-reflection phenomena have also been studied in detail [12–16]. However, in these GE configurations, reflected-shock/body interactions occur primarily on the ground-facing side; consequently, the resulting pressure changes remain largely confined to that side. This feature makes the observed aerodynamic mechanism somewhat similar to that of two-dimensional high-speed GE, where the dominant pressure variation generally occurs on the lower surface.

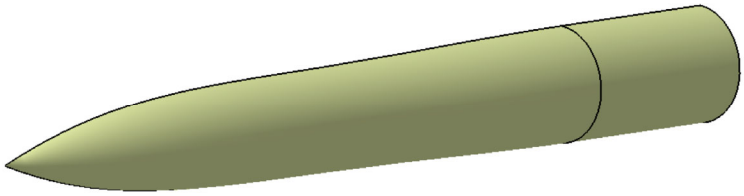
In aerodynamic interference studies involving multiple slender bodies, another shock-related mechanism, namely shock diffraction, has also received attention, although shock diffraction has primarily been studied in inherently unsteady configurations [17–20]. In contrast, studies of high-speed interference between slender bodies have shown that the flowfield is governed not only by incident and reflected shocks, but also by shock diffraction around the receiver body [21,22]. This diffraction process can substantially alter the local pressure distribution, force and moment characteristics, and even the aerodynamic response of finned configurations [23]. Hooseria and Skews [24] further identified double-reflected and double-diffracted shock-wave systems between closely spaced slender bodies, providing direct evidence of complex three-dimensional shock-diffraction mechanisms.

Nevertheless, high-speed GE studies to date have mainly focused on two-dimensional airfoils or relatively short projectiles, for which the aerodynamic influence of ground-reflected shocks is largely concentrated on the ground-facing side. The possible diffraction of ground-reflected shock waves around a high-fineness-ratio slender body, and its influence on the lateral and upper-surface pressure distributions, remain insufficiently understood. This issue is particularly relevant to missile-like configurations, whose extended axial length may promote more complex three-dimensional shock interactions than those observed for short projectiles. Therefore, the present study investigates the supersonic GE aerodynamics and flow characteristics of a slender body of revolution at different Mach numbers and heights, with particular emphasis on the reflection and diffraction mechanisms of ground-reflected shock waves around the body.

2. Numerical Method and Validation

2.1 Physical Model

The slender body model used in this study is based on the missile model from reference [4]. To ensure the general applicability of the results, the body is scaled to a length of $l = 1.0\ \mathrm{m}$ and a diameter of $d = 0.12\ \mathrm{m}$, with an angle of attack of $\alpha = 0°$. The half-body model used is shown in Figure 1. The freestream Mach number takes six representative supersonic values, Ma = 1.3, 1.5, 2.0, 3.0, 4.0, and 5.0, spanning low- supersonic to high-supersonic flow regimes. The corresponding Reynolds number ranges from $Re = 3.0 \times 10^7$ to $Re = 1.2 \times 10^8$. The relative flight height h/l changes from 0.5 to 0.05, and the unbounded flow field is denoted as $h/l = \infty$. The origin of the wind-axis coordinate system is located at the leading edge of the body, with the positive x-axis aligned with the freestream direction and the positive y-axis pointing upward.



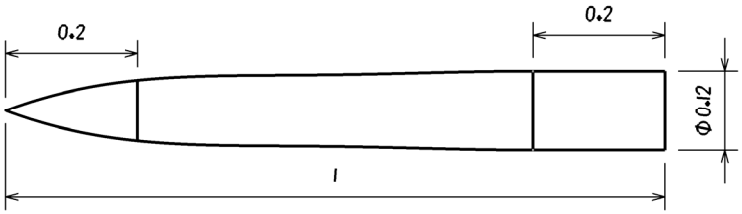


Figure 1 – Slender body half-model and parameters (in meters).

2.2 Numerical Method

A rectangular computational domain is used as shown in Figure 2. To examine the sensitivity of the results to the far-field boundary locations, the aerodynamic forces acting on the slender body are evaluated for a representative GE case at $Ma = 1.5$ and $h/l = 0.3$. The results are listed in Table 1. The aerodynamic forces are insensitive to the far-field boundary locations, with nearly identical aerodynamic loads obtained for different far-field distances. Therefore, to preserve the integrity of the ground-effect-related shock structures, the top, side, and outlet boundaries are located $3l$, $3l$ and $6l$ away from the body, respectively. The inlet boundary is l upstream of the body for the supersonic cases with a bow shock, and the bottom boundary is located a distance h below the trailing edge of the body. The pressure far-field boundary condition is employed for the inlet, side, outlet, and top boundaries. For the GE cases, the bottom boundary is treated as a no-slip moving wall with a translational velocity equal to the freestream velocity; for the unbounded-flow cases, it is also treated as a pressure far-field boundary. The initial mesh contains approximately 31 million cells, and the first cell height on the body surface is chosen to satisfy $y^+ \approx 1$.

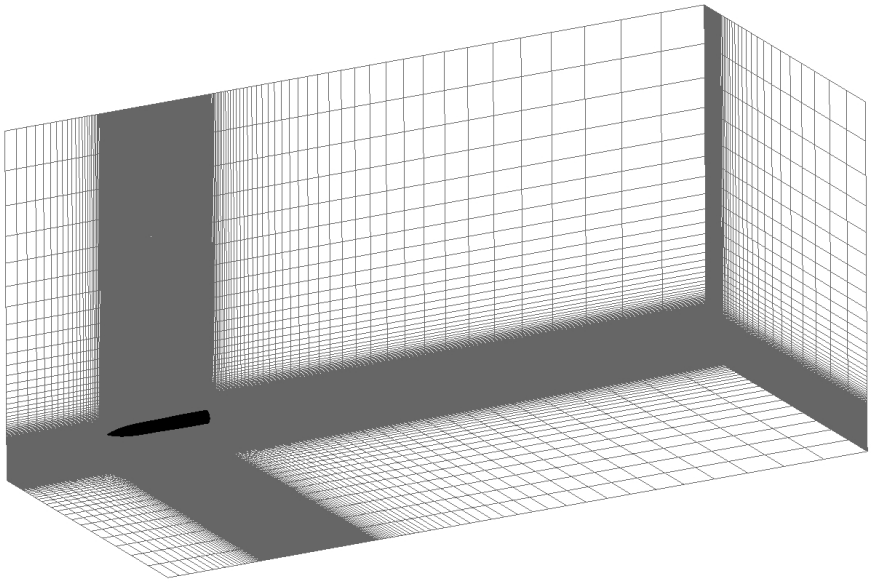


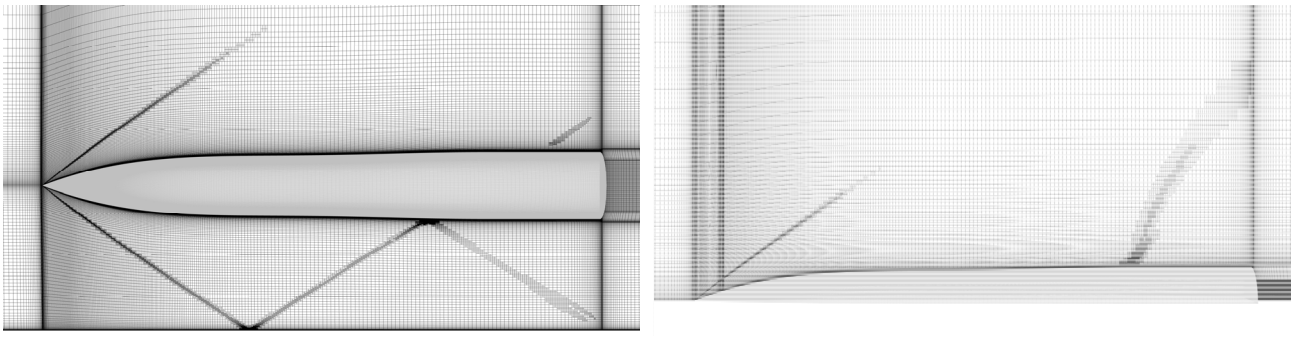
Figure 2 – Rectangular computational domain.

Table 1 – Effect of variations in far-field boundary locations for the half-body model

Domain extent, normalized by body length (U=upstream, D=downstream, S=side, T=top)	C_L	C_D	C_M
0.5U, 3D, 1.5S, 1.5T	0.01501	0.3499	-0.00768
1U, 6D, 3S, 3T	0.01502	0.3499	-0.00768
2U, 12D, 6S, 6T	0.01504	0.3499	-0.00767

The double-precision density-based solver in ANSYS FLUENT 2023R1 is used to perform the numerical simulations. The steady compressible Reynolds-averaged Navier–Stokes equations with the SST k-ω turbulence model are solved using the finite volume method. The ideal-gas model is adopted to account for compressibility, and the freestream density is specified at sea-level conditions. The Roe flux-difference splitting scheme is applied, with a second-order upwind scheme for the convection terms and a second-order central-difference scheme for the diffusion terms. To improve solution accuracy and convergence, three numerical correction methods are enabled: Warped-Face

Gradient Correction, High Order Term Relaxation, and Convergence Acceleration for Stretched Meshes. Because the shock thickness is much smaller than the grid spacing, mesh adaptation is applied to refine the region near the shock-wave surfaces. The refined mesh contains approximately 42 million cells, as shown in Figure 3. All cases are run until the variations in the forces and moments acting on the body become negligible (less than 0.1% over 1000 iterations), indicating that the flowfield is steady.



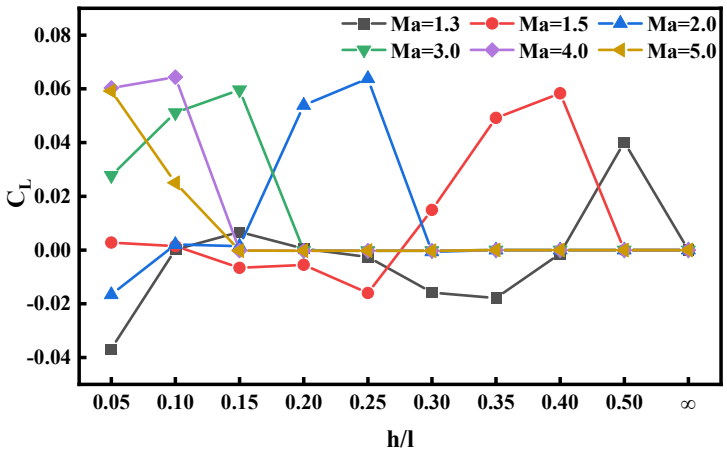
(a) The plane $z = 0$ (b) The plane $y = 0$

Figure 3 – Shock-adapted mesh.

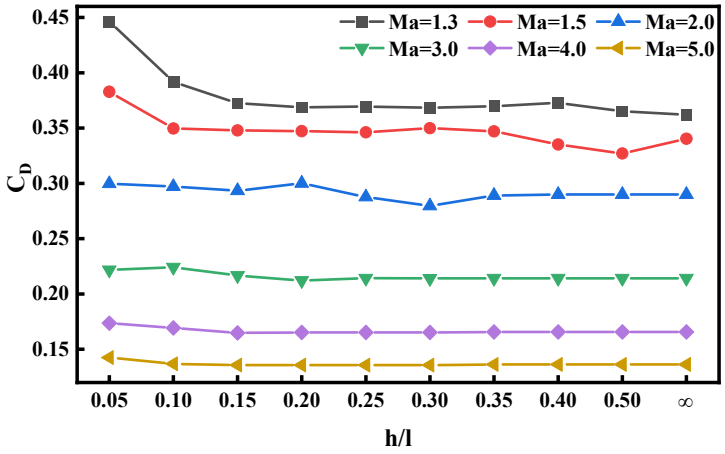
3. Results and Discussion

3.1 Aerodynamic Forces

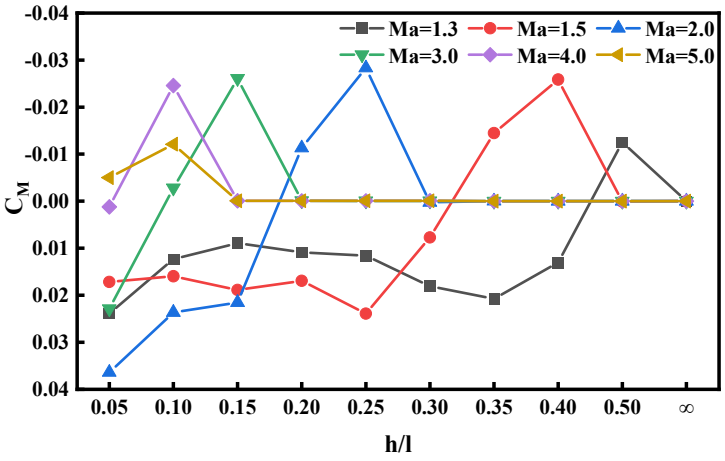
The aerodynamic coefficients at different Mach numbers and flight heights are shown in Figure 4. As the height decreases from the unbounded condition, the lift first increases from zero to a positive peak and then gradually decreases. For $Ma \leq 2.0$, the lift eventually becomes negative at smaller heights. The height corresponding to the lift peak decreases with increasing Mach number; at $Ma = 1.3$, this peak may occur at a height larger than $0.5l$. Compared with lift, the variation in drag is much less pronounced. As the height decreases, a slight drag trough appears before the lift begins to vary markedly, followed by a small drag peak. More pronounced drag variations are observed only at very low heights for $Ma \leq 1.5$. The pitching moment exhibits a trend closely related to the lift variation: the maximum nose-up moment occurs near the height of peak lift, after which the moment decreases rapidly and becomes nose-down. Overall, the effective range of GE decreases progressively as the Mach number increases, owing to the gradual reduction in the shock-wave angle.



(a) Lift coefficient



(b) Drag coefficient



(c) Moment coefficient

Figure 4 – Aerodynamic force curves with flight height at different Mach numbers.

3.2 Flow Field

The pressure distribution over the slender body is analyzed first. Unlike two-dimensional GE aerodynamics, in which the surface pressure is usually examined only along the upper and lower surfaces, three-dimensional GE requires consideration of the pressure variation over the entire circumferential surface of the body. The side view provides an intuitive visualization of the overall surface pressure distribution. However, the pressure variations near the upper and lower meridians, which make major contributions to the aerodynamic forces, cannot be clearly identified from the side view, as shown in Figure 5. Therefore, to facilitate the analysis of circumferential pressure variation, the circumferential angle ϕ is defined on the rear-view cross section of the body, as illustrated in Figure 6. Here, ϕ denotes the azimuthal angle around the body surface. Based on this definition, the surface of the body of revolution is unwrapped into a two-dimensional rectangular map in the $x/l - \phi$ plane, as shown in Figure 7. This representation makes it possible to identify the pressure footprints induced by GE shock interactions over the entire body surface, especially in the windward and leeward regions that are closely related to lift generation.

At the representative Mach number of $Ma = 2.0$ in Figure 7, the GE-induced pressure variation exhibits a clear dependence on height. As the height decreases, the GE-induced pressure change first appears near the lowermost region of the body tail at $h/l = 0.30$. When the height is further reduced to $h/l = 0.25$, the increased-pressure region expands mainly over the $\phi \leq 0$ side, leading to an increase in lift. At $h/l = 0.20$, this high-pressure region extends toward the $\phi \geq 0$ side, which partly

offsets the lift-producing pressure increment. With a further decrease in height, the high-pressure region moves progressively upstream and its magnitude increases. Meanwhile, a negative pressure-increment region appears downstream of the high-pressure region, mainly over the $\phi \leq 0$ side, and gradually expands as the height decreases. This negative pressure-increment region is responsible for the subsequent decrease in lift.

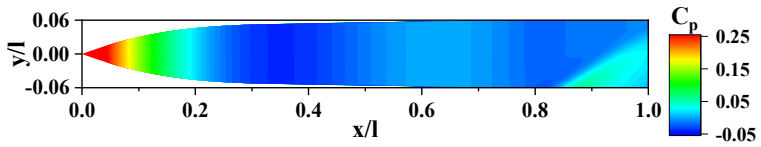


Figure 5 – Side view of the surface pressure distribution at $Ma = 2.0$, $h/l = 0.25$.

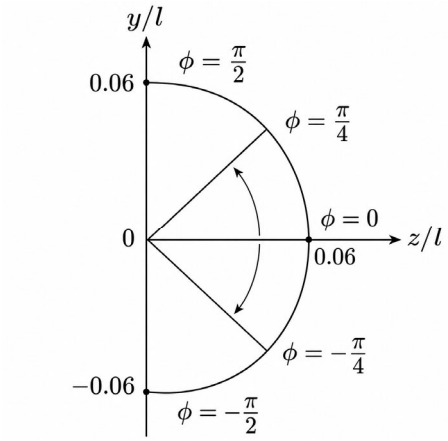
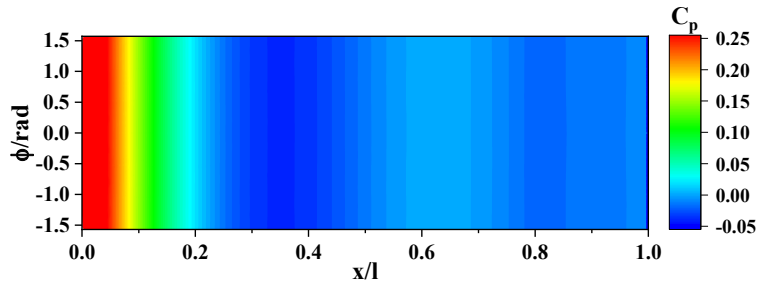
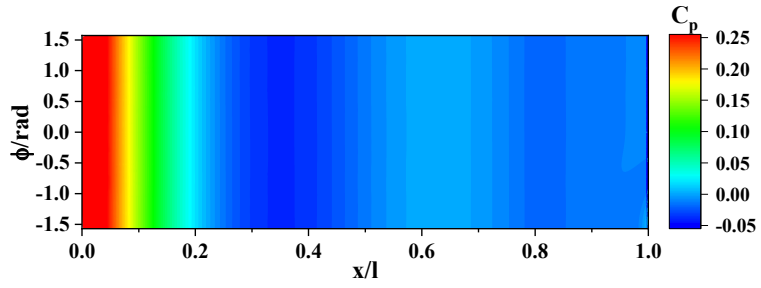


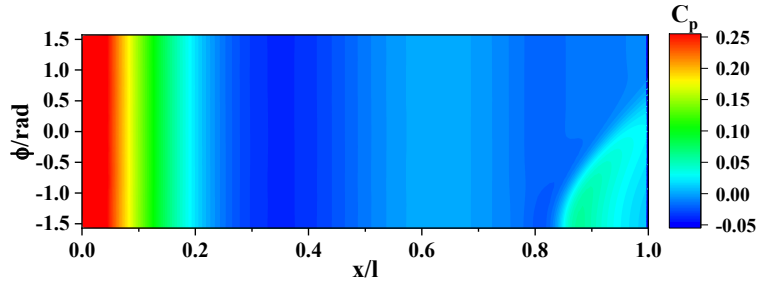
Figure 6 – Definition of the circumferential angle ϕ on the rear-end base cross section of the slender body.



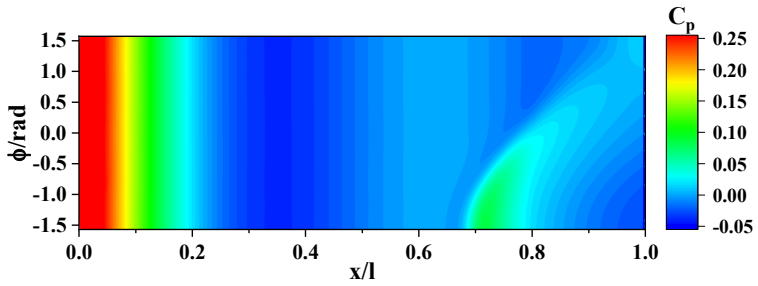
(a) $h/l = \infty$



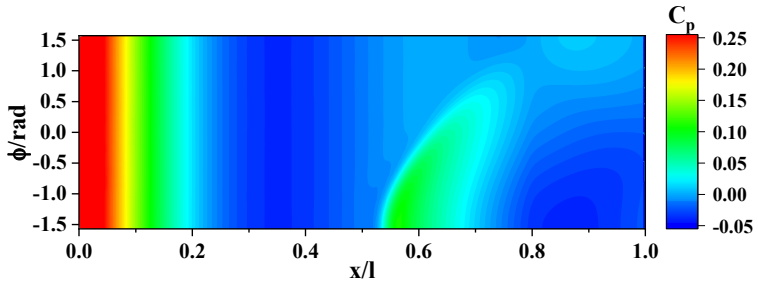
(b) $h/l = 0.30$



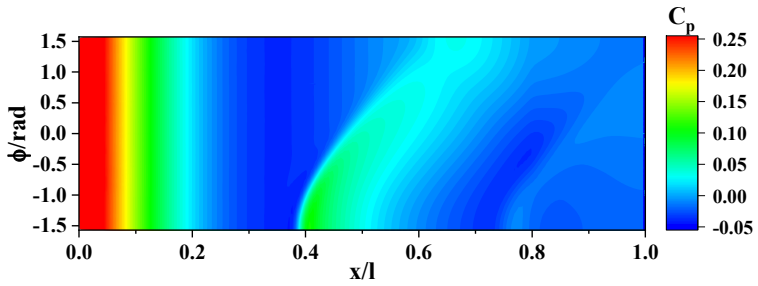
(c) $h/l = 0.25$



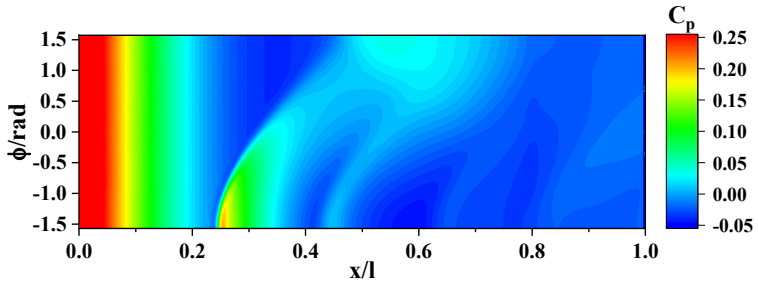
(d) $h/l = 0.20$



(e) $h/l = 0.15$



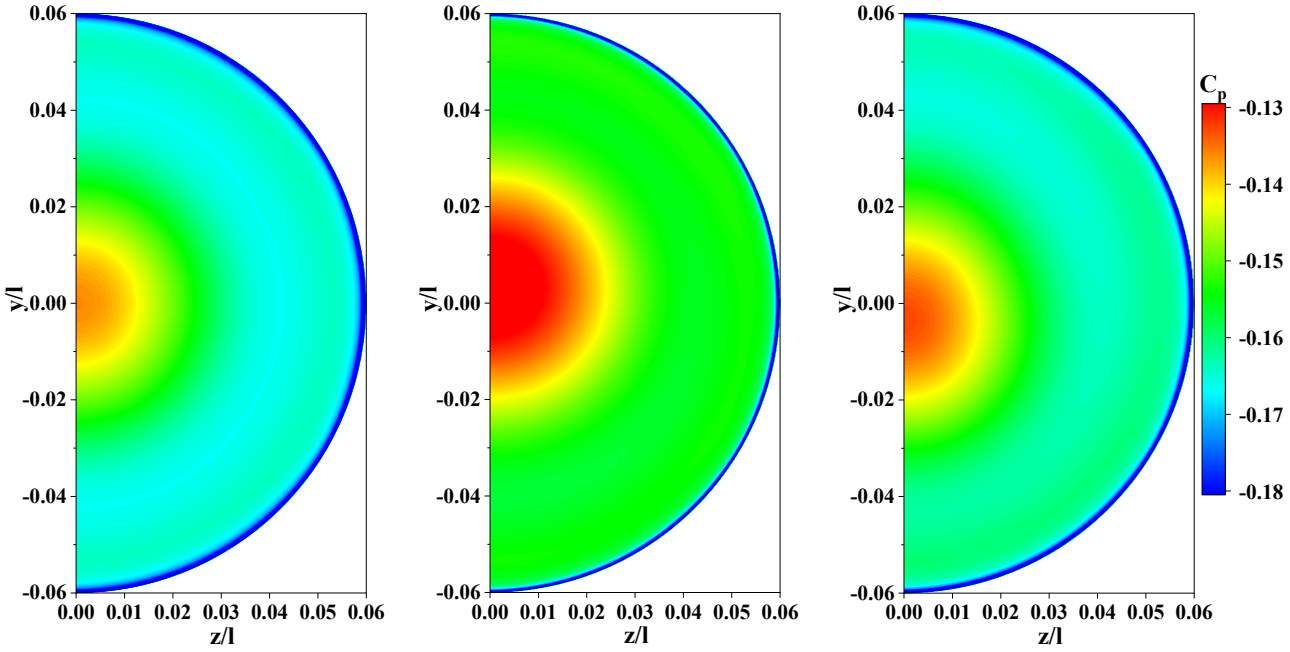
(f) $h/l = 0.10$



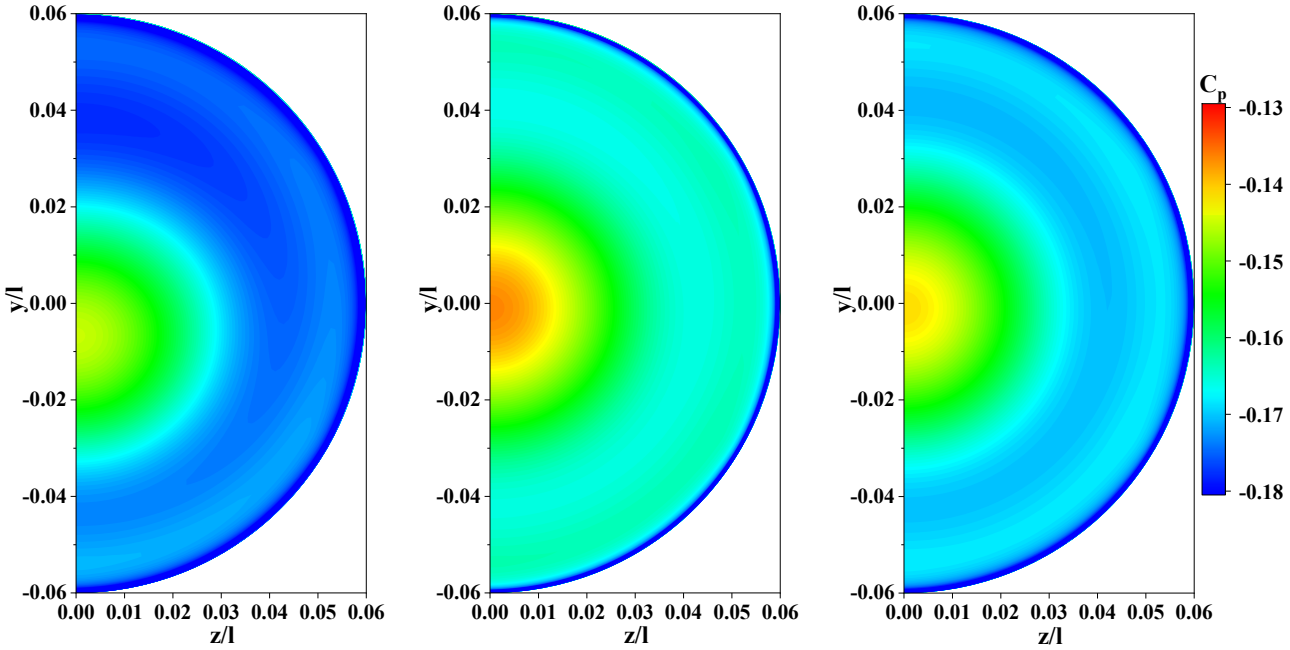
(g) $h/l = 0.05$

Figure 7 – Surface-unwrapped pressure distribution in the $x/l - \phi$ plane at $Ma = 2.0$.

The drag variation can also be interpreted from the evolution of the surface pressure distribution. For $Ma = 2.0$, most of the pressure variation occurs over the surface region with $x/l \geq 0.2$, where the local body surface is nearly parallel to the x-axis. As a result, the pressure-induced axial-force component is small, and the drag remains nearly unchanged. The pressure distribution on the rear-end base face has a more direct influence on the axial force. As shown in Figure 8, the base-face pressure increases at $h/l = 0.30$, then gradually decreases and reaches a minimum at $h/l = 0.20$, before recovering as the height is further reduced. However, because the variation in base-face pressure is relatively small, it does not induce a pronounced change in drag, even though the corresponding pressure force is aligned with the x-axis. A marked drag increase occurs only when the high-pressure region moves upstream to the forebody region with $x/l < 0.2$, where the local surface inclination is larger and the pressure rise contributes more directly to the axial force, as shown in Figure 9(b).

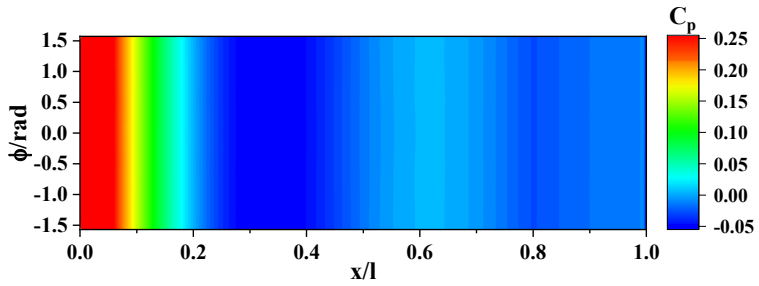


(a) $h/l = \infty$ (b) $h/l = 0.30$ (c) $h/l = 0.25$

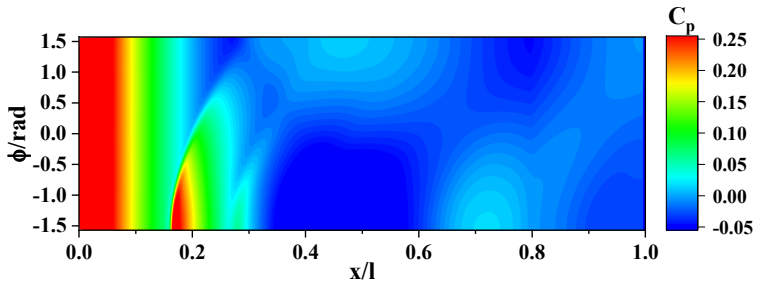


(d) $h/l = 0.20$ (e) $h/l = 0.15$ (f) $h/l = 0.10$

Figure 8 – Pressure distribution on the rear-end base face at $Ma = 2.0$.



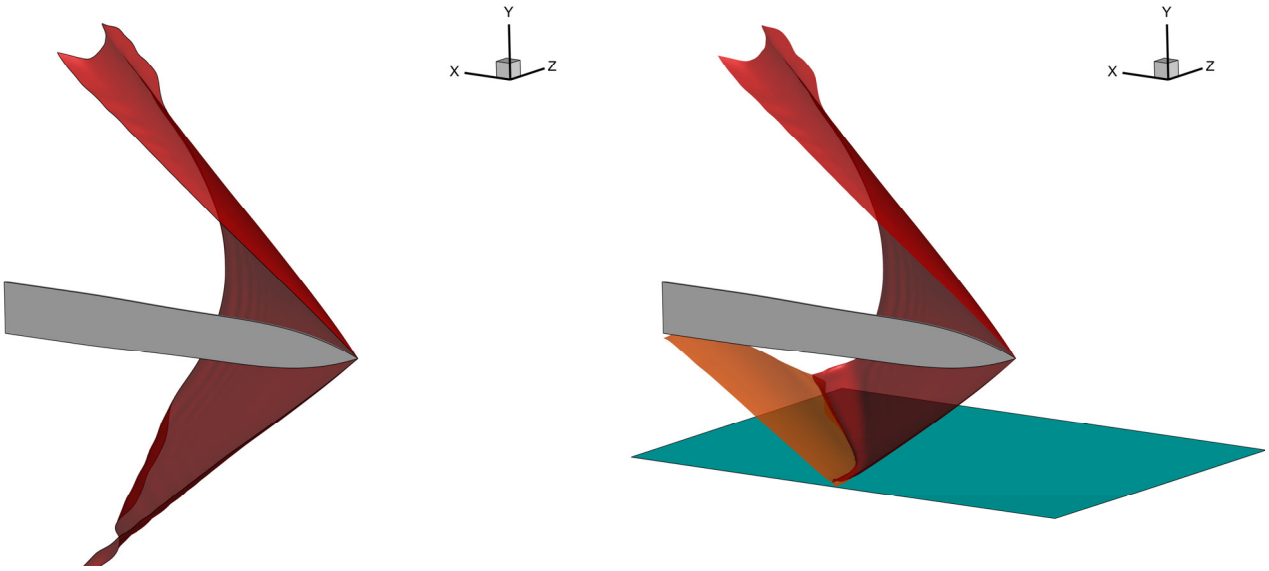
(a) $h/l = \infty$



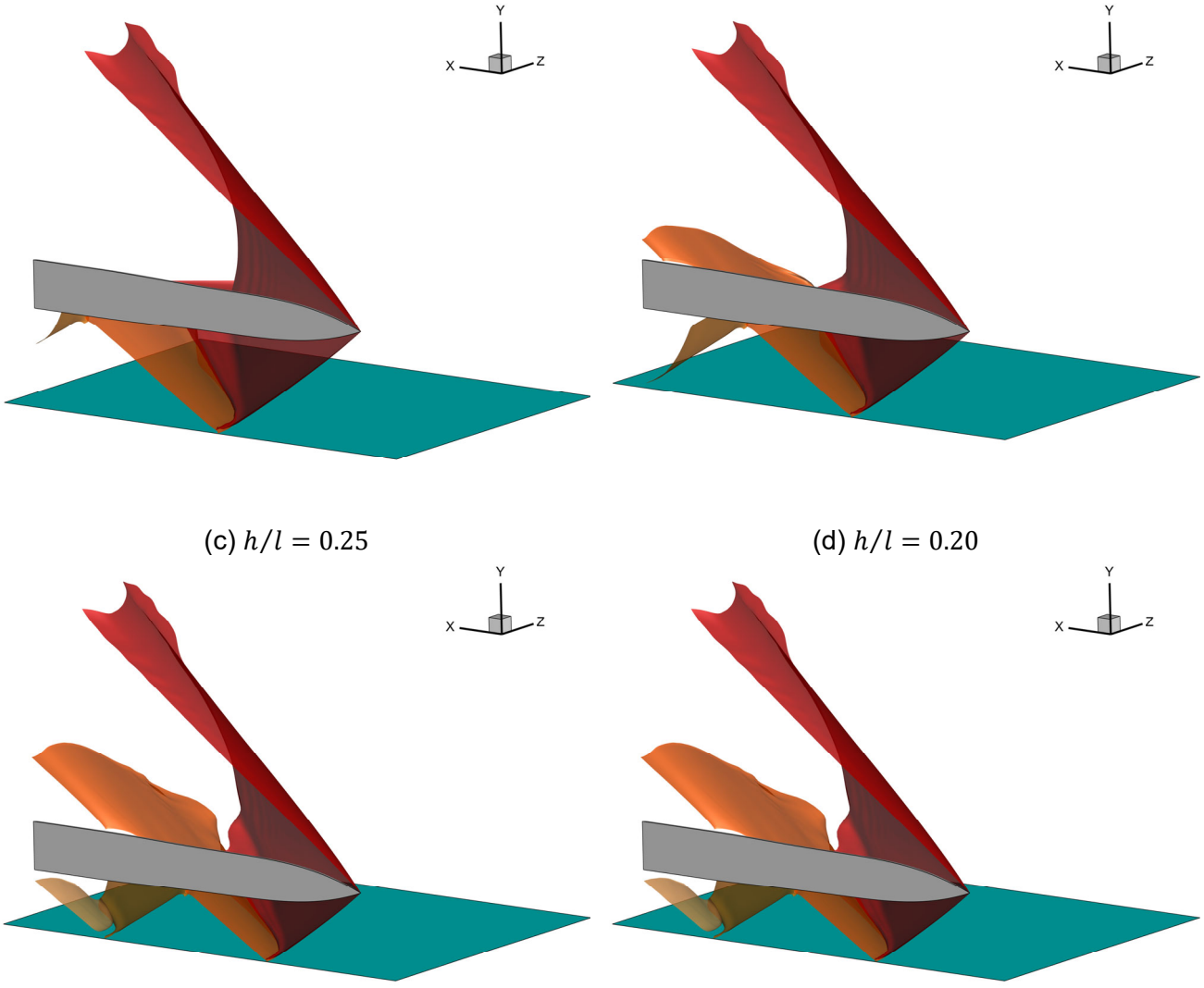
(b) $h/l = 0.05$

Figure 9 – Surface-unwrapped pressure distribution in the $x/l - \phi$ plane at $Ma = 1.5$.

To further relate the pressure footprints to the underlying shock structures, the shock surfaces are extracted from the density-gradient field to identify the nose-generated conical shock surface and its successive reflected shock surfaces, as shown in Figure 10. At $h/l = 0.30$, the primary ground-reflected shock surface passes close to the wake region and therefore affects the pressure distribution on the rear-end base face to some extent. When the height is reduced to $h/l \leq 0.25$, the ground-reflected shock impinges on the body and forms a secondary body-reflected shock surface. This shock impingement produces a marked pressure rise mainly over the $\phi \leq 0$ side of the body. As the height is further decreased, the reflected shock undergoes pronounced diffraction around the body surface, causing the high-pressure region to extend toward the $\phi \geq 0$ side. In addition, the secondary body-reflected shock surface is reflected again by the ground, forming a tertiary ground-reflected shock surface. For $h/l \leq 0.10$, this tertiary reflected shock propagates back to the body and generates a quaternary body-reflected shock surface. These successive shock reflections and diffraction explain the upstream movement and circumferential expansion of the GE-induced pressure variations as the body approaches the ground.



(a) $h/l = \infty$ (b) $h/l = 0.30$

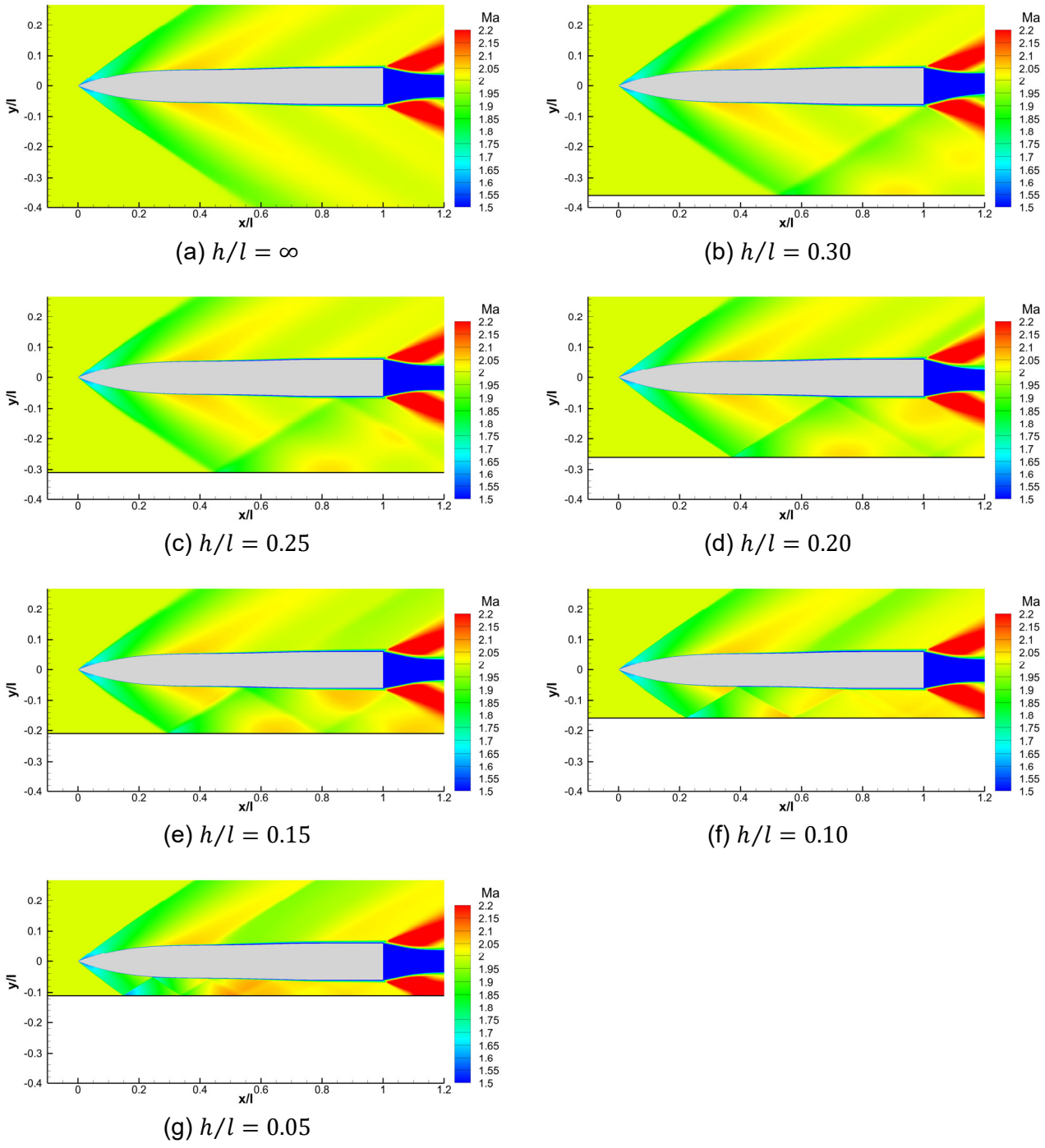


(c) $h/l = 0.25$ (d) $h/l = 0.20$

(e) $h/l = 0.15$ (f) $h/l = 0.10$

Figure 10 – Shock surfaces at different heights for $Ma = 2.0$.

Although the shock surfaces exhibit pronounced three-dimensional spatial distributions, the symmetry plane remains the most representative section for interpreting the main flow features. Therefore, the Mach-number contours on the symmetry plane are examined, as shown in Figure 11. At $h/l = 0.30$, the wake is deflected upward under the influence of the ground-reflected shock. In addition, an expansion wave is generated near $x/l = 0.2$ on the body surface, leading to local flow acceleration. This expansion wave is also reflected between the body and the ground and is responsible for the negative pressure increment observed on the body. At $h/l = 0.20$, the wake is instead deflected downward under the influence of the reflected expansion wave. Unlike shock waves, the expansion wave is less spatially concentrated and does not exhibit pronounced diffraction toward the upper meridian. As a result, the associated pressure reduction mainly remains on the lower side of the body, thereby producing a negative lift contribution.



(a) $h/l = \infty$ (b) $h/l = 0.30$

(c) $h/l = 0.25$ (d) $h/l = 0.20$

(e) $h/l = 0.15$ (f) $h/l = 0.10$

(g) $h/l = 0.05$

Figure 11 – Mach-number contours at different heights for $Ma = 2.0$.

4. Conclusions

This study investigated the supersonic ground-effect aerodynamics of a high-fineness-ratio slender body of revolution using steady compressible Reynolds-averaged Navier–Stokes simulations. The effects of Mach number and flight height on the aerodynamic characteristics were analyzed, and the underlying three-dimensional flow mechanisms were clarified. The results showed that, as the body approached the ground, the lift initially increased and reached a positive peak before decreasing rapidly; at lower supersonic Mach numbers, the lift eventually became negative at small clearances. In contrast, the drag variation was relatively weak over most height ranges and increased noticeably only under extremely low-clearance conditions. The effective range of ground effect was found to decrease with increasing Mach number due to the reduction in shock-wave angle.

The flowfield analysis revealed that the aerodynamic variations were primarily associated with successive shock reflections between the body and the ground, as well as the diffraction of ground-reflected shocks around the slender body. These three-dimensional shock interactions produced

complex circumferential pressure redistribution over the body surface, governing the changes in lift and pitching moment. The present results provide new insights into the near-ground aerodynamic behavior of missile-like slender vehicles in supersonic flight and highlight the importance of three-dimensional shock diffraction effects in high-speed ground-effect flows.

5. Contact Author Email Address

Corresponding author: Yiyuan Xun

Email: xunyu@buaa.edu.cn

6. Copyright Statement

The authors confirm that they, and/or their company or organization, hold copyright on all of the original material included in this paper. The authors also confirm that they have obtained permission, from the copyright holder of any third party material included in this paper, to publish it as part of their paper. The authors confirm that they give permission, or have obtained permission from the copyright holder of this paper, for the publication and distribution of this paper as part of the ICAS proceedings or as individual off-prints from the proceedings.

References

[1] Qu Q, Wang W, Liu P and Agarwal RK. Airfoil aerodynamics in ground effect for wide range of angles of attack. *AIAA Journal*, Vol. 53, No. 4, pp 1048–1061, 2015.

[2] Shi X, Qu Q, Liu P, Xun Y, Bu C and Chen H. Feasibility analysis of fixed plates in chord-dominated static ground effect wind-tunnel experiment. *AIAA Journal*, Vol. 60, No. 9, pp 5286–5298, 2022.

[3] Doig G. Transonic and supersonic ground effect aerodynamics. *Progress in Aerospace Sciences*, Vol. 69, pp 1–28, 2014.

[4] Ye N, Long T, Meng J, Shi R and Zhang B. Surrogate-assisted optimization for anti-ship missile body configuration considering high-velocity water touching. *Chinese Journal of Aeronautics*, Vol. 36, No. 12, pp 268–281, 2023.

[5] Doig G, Barber TJ, Neely AJ and Myre DD. Aerodynamics of an aerofoil in transonic ground effect: numerical study at full-scale Reynolds numbers. *The Aeronautical Journal*, Vol. 116, No. 1178, pp 407–430, 2012.

[6] Gao B, Qu Q and Agarwal RK. Aerodynamics of a transonic airfoil in ground effect. *Journal of Aircraft*, Vol. 55, No. 6, pp 2240–2255, 2018.

[7] Jiang W, Hu S, Jiang C and Lee C-H. Choking limit prediction for diamond airfoils in supersonic ground effect. *Journal of Fluid Mechanics*, Vol. 1033, A16, 2026.

[8] Carriage K, Young J, Kleine H and Hiraki K. Reynolds-averaged Navier-Stokes computation of transonic projectiles in ground effect. *Proceedings of the 18th Australasian Fluid Mechanics Conference*, Launceston, Australia, 2012.

[9] Doig G, Wang S, Kleine H and Young J. Aerodynamic analysis of projectiles in ground effect at near-sonic Mach numbers. *AIAA Journal*, Vol. 54, No. 1, pp 150–160, 2016.

[10] Doig G, Barber TJ, Leonardi E, Neely AJ and Kleine H. Aerodynamics of a supersonic projectile in proximity to a solid surface. *AIAA Journal*, Vol. 48, No. 12, pp 2916–2930, 2010.

[11] Sheridan C, Young J, Kleine H, Hiraki K and Nonaka S. Ground effect of transonic and supersonic projectiles: influence of Mach number and ground clearance. *Proceedings of the 30th International Symposium on Shock Waves*, pp 635–640, 2017.

[12] Gaitonde DV and Adler MC. Dynamics of three-dimensional shock-wave/boundary-layer interactions. *Annual Review of Fluid Mechanics*, Vol. 55, pp 291–321, 2023.

[13] Zuo F-Y and Pirozzoli S. Recent progress in conical shock wave/boundary layer interaction with spanwise pressure gradient. *Propulsion and Power Research*, Vol. 13, No. 3, pp 295–318, 2024.

[14] Skews BW. Three-dimensional effects in wind tunnel studies of shock wave reflection. *Journal of Fluid Mechanics*, Vol. 407, pp 85–104, 2000.

[15] Xiang GX, Wang C, Teng HH and Jiang ZL. Investigations of three-dimensional shock/shock interactions over symmetrical intersecting wedges. *AIAA Journal*, Vol. 54, No. 5, pp 1472–1481, 2016.

[16] Surujhlal D and Skews BW. Three-dimensional shock wave reflection transition in steady flow. *Journal of Fluid Mechanics*, Vol. 858, pp 565–587, 2019.

[17] Abate G and Shyy W. Dynamic structure of confined shocks undergoing sudden expansion. *Progress in Aerospace Sciences*, Vol. 38, No. 1, pp 23–42, 2002.

[18] Keller JB and Blank A. Diffraction and reflection of pulses by wedges and corners. *Communications on Pure and Applied Mathematics*, Vol. 4, No. 1, pp 75–94, 1951.

[19] Bryson AE and Gross RWF. Diffraction of strong shocks by cones, cylinders, and spheres. *Journal of Fluid*

Mechanics, Vol. 10, No. 1, pp 1–16, 1961.

[20] Reeves JO and Skews BW. Unsteady three-dimensional compressible vortex flows generated during shock wave diffraction. *Shock Waves*, Vol. 22, No. 2, pp 161–172, 2012.

[21] Derunov EK, Volkov VF, Zheltovodov AA and Maksimov AI. Analysis of supersonic flow around two bodies of revolution near a surface. *Thermophysics and Aeromechanics*, Vol. 16, No. 1, pp 13–35, 2009.

[22] Chaplin RA, MacManus DG and Birch TJ. Aerodynamic interference between high-speed slender bodies. *Shock Waves*, Vol. 20, No. 2, pp 89–101, 2010.

[23] Chaplin R, MacManus D, Leopold F, Martinez B, Gauthier T and Birch T. Aerodynamic interference on finned slender body. *AIAA Journal*, Vol. 54, No. 7, pp 2017–2033, 2016.

[24] Hooseria SJ and Skews BW. Shock wave interactions between slender bodies: some aspects of three-dimensional shock wave diffraction. *Shock Waves*, Vol. 27, No. 1, pp 109–126, 2017.